Nanoscale

Size-Controlled Nanocrystals Reveal Spatial Dependence and Severity of Nanoparticle Coalescence and Ostwald Ripening in Sintering Phenomena

Journal:	*Nanoscale*
Manuscript ID	NR-ART-11-2020-007960.R1
Article Type:	Paper
Date Submitted by the Author:	08-Dec-2020
Complete List of Authors:	Goodman, Emmett; Stanford University, Chemical Engineering Carlson, Evan; Stanford University, Chemical Engineering Dietze, Elisabeth; Karlsruhe Institute of Technology Tahsini, Nadia; Stanford University, Chemical Engineering Johnson, Arun; Stanford University, Chemical Engineering Aitbekova, Aisulu; Stanford University, Chemical Engineering Nguyen Taylor, Temy; Stanford University, Chemical Engineering Plessow, Philipp; Karlsruher Institut fur Technologie - Campus Nord, IKFT Cargnello, Matteo; Stanford University, Chemical Engineering

Size-Controlled Nanocrystals Reveal Spatial Dependence and Severity of Nanoparticle Coalescence and Ostwald Ripening in Sintering Phenomena

Authors: Emmett D. Goodman[1], Evan Z. Carlson[1], Elisabeth M. Dietze[2], Nadia Tahsini[1], Arun Johnson[1], Aisulu Aitbekova[1], Temy Nguyen Taylor[1], Philipp N. Plessow[2], Matteo Cargnello[1]*

[1]Department of Chemical Engineering and SUNCAT Center for Interface Science and Catalysis, Stanford University, Stanford CA, 94305, USA.

[2]Institute of Catalysis Research and Technology, Karlsruhe Institute of Technology, Hermann-von-Helmholtz-Platz 1, D-76344 Eggenstein-Leopoldshafen, Germany.

*Correspondence to: mcargnello@stanford.edu.

Abstract:

A major aim in the synthesis of nanomaterials is the development of stable materials for high-temperature applications. Although the thermal coarsening of small and active nanocrystals into less active aggregates is universal in material deactivation, the atomic mechanisms governing nanocrystal growth remain elusive. By utilizing colloidally-synthesized Pd/SiO_2 powder nanocomposites with controlled nanocrystal sizes and spatial arrangements, we unravel the competing contributions of particle coalescence and atomic ripening processes in nanocrystal growth. Through the study of size-controlled nanocrystals, we can uniquely identify the presence of either nanocrystal dimers or smaller nanoclusters, which indicate the relative contributions of these two processes. By controlling and tracking nanocrystal density, we demonstrate the *spatial-dependence* of nanocrystal coalescence, and the *spatial-independence* of Ostwald (atomic) ripening. Overall, we prove that the most significant loss of nanocrystal surface area is due to high-temperature atomic ripening. This observation is in quantitative agreement with changes in nanocrystal density produced by simulating atomic exchange. Using well-defined colloidal materials, we extend our analysis to explain the unusually high-temperature stability of Au/SiO_2 materials up to 800 °C.

Keywords: palladium, silica, sintering, Ostwald ripening, gold

Introduction

Structural stability is critically important in the development of industrially-relevant materials, yet is underemphasized in academic research.[1] In many applications involving polycrystalline solids or powders composites, high-temperature nanocrystal coarsening leads to deteriorated properties; in catalysis for example it decreases activity, changes selectivity, and leads to overall loss of productivity due to downtime associated with catalyst reactivation or replacement.[2,3] When reactivation is not possible, catalyst deactivation drives utilization of large quantities of catalytic material to ensure effective catalysis throughout the material's application.[4]

In powder catalysts especially, one of the most common and severe causes of deactivation is due to lost reactive surface area caused by particle growth. This process is known as sintering. Two mechanisms have been proposed: Ostwald (atomic) ripening, or the exchange of atoms between stationary nanocrystals (NCs); and particle migration and coalescence, or the collision and fusion of entire nanocrystals.[3,5] In the literature, there is a lack of experimental methods to distinguish between these mechanisms. *In-situ* microscopy offers a promising approach, but is low-throughput, requires controlled conditions, and extreme care must be taken to avoid spurious effects of the high-energy electron beam.[6] Additionally, the study of evolving particle size distributions in polydisperse catalysts has been identified as fruitless.[7] Approaches involving kinetic modeling may provide insight, but incorrect assumptions can create significant errors.[8] Overall, it has been challenging to identify, and therefore suppress, coarsening mechanisms in composite nanomaterials.

To combat any potential coarsening mechanism, researchers are continuously developing novel nanostructures in attempts to enhance materials stability. Common nanostructured motifs include encapsulation, nanocrystal embedding in nanochannels, and nanocrystal entrenchment into

nanobowls or other high-surface-area supports.[9–18] Nanostructured geometries aim to physically separate particles to minimize interparticle interactions and maximize particle stability. However, such schemes often result in decreased overall activity due to mass-transfer limitations or reduced reactive surface area. A description of the specific sintering processes would allow for the intelligent design of nanostructures which target a specific deactivation mechanism.

In this work, by combining colloidally-synthesized powder nanomaterials and quantitative simulation studies, we provide new fundamental insights into materials stability. By precisely controlling nanocrystal size (3.0, 9.1, and 15.8 nm) and nanocrystal density (from 2 NC μm^{-2} to 367 NC μm^{-2}) we uncover the unique size- and density-dependences of particle growth processes. At lower temperatures, a *density-dependent* nanoparticle coalescence occurs, which is evidenced by direct observation of a bimodal particle size distribution. However, at higher temperatures, nanocrystal growth is dominated by *density-independent* Ostwald ripening, which is directly observed via the emergence of small nanoclusters. This latter process represents the most severe loss of nanocrystal surface area, and was found to be in quantitative agreement with simulations of a metallic vapor-phase sintering process. By observing nanocrystal growth to be independent of nanocrystal spatial distribution, we identify atomic emission as the critical process controlling nanocrystal growth and, therefore, sintering processes. Finally, we demonstrate that simulations of vapor-phase atomic exchange also predict the behavior of Au/SiO_2 composites, which maintain unusually remarkable stability up to 800 ºC.

Results and Discussion

Synthesis and Characterization of Well-Defined Nanocrystal Ensembles. To disentangle the effects of nanocrystal size and spatial distribution on materials stability, we used a

colloidal assembly approach where pre-formed Pd or Au nanocrystals were deposited onto pre-formed SiO_2 spheres. The key advantages of this building-block approach are: (1) a highly uniform active phase which allows probing of size-dependent sintering properties; (2) well-defined initial particle sizes, which allow particle size measurements to indicate sintering mechanism (vide infra); and (3) independent control of the size and spatial distribution of NCs, to study the effect of spatial parameters on materials stability. Here, we synthesized size-controlled 3.0 ± 0.3 nm, 9.1 ± 0.5 nm, and 15.8 ± 1.3 nm Pd nanocrystals as active phases (**Figure 1a-c**), and monodisperse 232 nm Stober SiO_2 spheres as the supporting oxide phase. Controlled assembly of Pd nanocrystals onto colloidal SiO_2 was performed by impregnation in solution, such that Pd was well-dispersed on the surface of each SiO_2 sphere (**Figures 1d-f, Supporting Figures S1-S3**). Although transmission electron microscopy (TEM) measurements may show overlap between Pd NCs, this effect is due to the 2D projection nature of microscopy images for particles lying on opposite sides of the SiO_2 spheres. High-angular annular dark field scanning tunneling electron microscopy (HAADF-STEM) tomography demonstrates the random distribution of Pd NCs on the overall SiO_2 surface (**Supporting Figure S4**). Measurements of Pd nanocrystal size as-synthesized and after assembly onto the SiO_2 surface confirm the uniformity of the Pd phase, although a slight decrease in size is observed due to different wetting properties of Pd on carbon with respect to silica (**Figure 1g-i**). Pd loading and additional characterization for each nanocomposite are reported in **Supporting Table S1**.

Additionally, for some materials various NC loadings were synthesized to investigate the effects of nanoparticle proximity. These materials are labeled N-Pd/SiO_2, where N represents the average number of Pd NCs per SiO_2 sphere. Representative TEM images of the four materials are shown in **Supplementary Figure S5**, where we observe different NC spatial distribution but

maintained NC size. The NC loadings are quantified by tallying the number of Pd NCs per SiO_2 sphere over many Pd/SiO_2 structures within a sample, and these statistics are shown in **Supporting Figure S5**. Consequently, the four materials are labelled as 0.3-Pd/SiO_2, 4.0-Pd/SiO_2, 17-Pd/SiO_2, and 62-Pd/SiO_2, after the average number of Pd NCs per SiO_2 sphere. By computationally simulating this random NC deposition process and modeling a large number of spheres with a given number of Pd NCs on their surface, we can calculate the distribution of nearest neighbor distances for each sample, a parameter crucial to processes where interparticle diffusion governs the material stability (**Supporting Figure S6**).[16] As the average nearest neighbor distance between NCs varies from 26 nm to 173 nm along the sample series, we expect these materials to possess different stability properties if surface diffusional processes dominate. Additionally, these Pd/SiO_2 nanocomposites represent localized support surfaces where particles may sinter, as there are significant barriers to atomic transfer between spheres.[19]

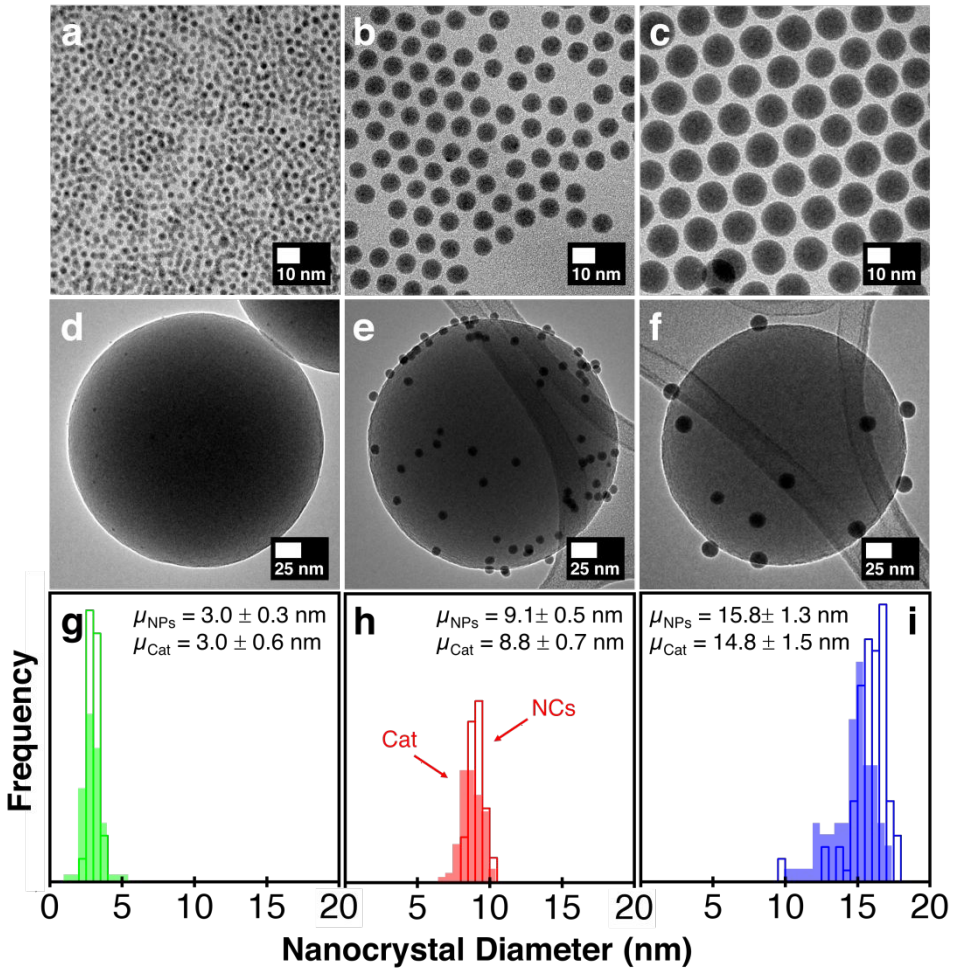

Figure 1. **Size-Controlled Nanocomposites.** Transmission electron microscopy (TEM) images of three sizes of (a-c) as-synthesized colloidal Pd nanocrystals and (d-f) corresponding SiO_2-supported Pd nanocrystals. Particle size distributions (g-i) of as-synthesized nanocrystal (open bars) and SiO_2-supported nanocrystals (closed bars). Mean values and standard deviations shown for as-synthesized nanocrystals (μ_{NCs}) and SiO_2-supported nanocrystals (μ_{Cat}).

Thermal Stability Studies. The prepared materials were used to study the size-dependent Pd stability after calcination in air. The SiO_2 support spheres are stable in air up to at least 925 °C and therefore remain stable under the conditions investigated in this work. For each nanocomposite, we measure the mean nanocrystal diameter after aging at increasing temperature (**Figure 2**).

Between room temperature and 800 ºC, we observe a slight increase in nanocrystal size for all three materials, which we identify as density-dependent oxidative particle coalescence (vida infra). However, between 888 °C and 900 °C, the mean diameter of the 3.0 nm and 8.8 nm samples increased dramatically to ~30 nm. The fact that these samples show particle growth at approximately the same temperature (within 15 °C) is surprising given that smaller particles are usually considered having a much higher driving force to sinter due to their higher surface energy.[20] Once 3.0 nm Pd begins to sinter, the number of NCs per SiO_2 sphere dramatically falls, and very few yet large Pd aggregates were observable. Although the 14.7 nm sample also produced numerous larger aggregates between 888 °C and 900 °C, the mean particle diameter slightly decreased, which gives fundamental insight into the mechanism of particle growth (vide infra). Overall, all NC sizes produce very large sintered aggregates at 888 °C, and this temperature represents a critical turning point in the stability of the Pd/SiO_2 materials.

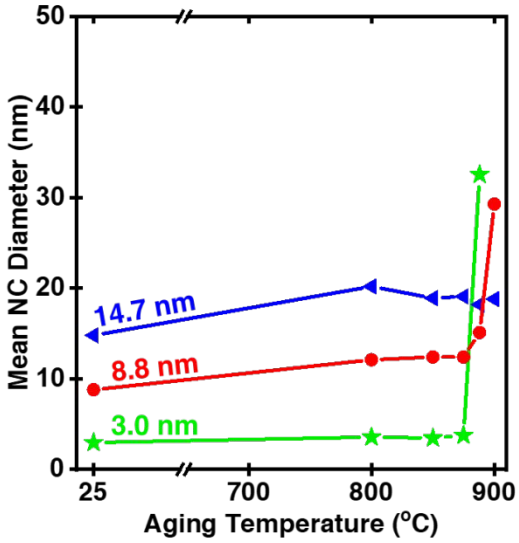

Figure 2. Size-Dependent Stability of Pd/SiO_2 Materials. Mean NC diameter versus aging temperature for 3.0 nm, 8.8 nm, and 14.7 nm Pd/SiO_2 nanocomposites.

To understand the increase in NC size between 25 °C and 800 °C, we studied nanocrystal projected areas before and after aging at 800 °C for the 8.8 nm 62-Pd/SiO_2 nanocomposite (**Figure 3**). Interestingly, we see that the originally monodisperse distribution centered around 64 nm^2 (~9.0 nm diameter) of NC areas transitions to a bimodal distribution with peaks at 80 nm^2 (~10.1 nm diameter) and 161 nm^2 (~14.3 nm diameter). The fact the second peak in the bimodal area distribution is centered at two times the larger peak suggests the formation of dimers due to entire particle coalescence, which would result in peak distributions located at integer values of the original NC size. This phenomenon is only observable with highly uniform nanocrystals, as polydisperse catalysts would reveal smooth monomodal particle size distributions regardless of the growth mechanism.[7] Furthermore, various NC densities were studied in a similar manner, and particle coalescence was found to be most severe in the catalyst with the highest NC density (62 NCs/SiO_2), where ~35% (**Supporting Figure S7**) of the original NCs coalescence to form dimers (and even some trimers). Given the well-defined particle densities and support surface areas, Monte Carlo simulations suggest that these fusion percentages are achievable if each particle translates on the support at most 8 nm from its original starting location (**Supporting Figure S7)**. The fact that we do not observe extensive particle coalescence in the 3.0 nm Pd/SiO_2 materials suggests the occurrence of a simultaneous nanocrystal oxidation and coalescence, rather than multiple steps of NC diffusion, as the main particle coalescence mechanism. These materials are broadly stable above their Tamman temperature, which suggests that this measure of bulk-mobility is not a sufficient predictor to anticipate when significant nanocrystal growth may occur on a support.[2]

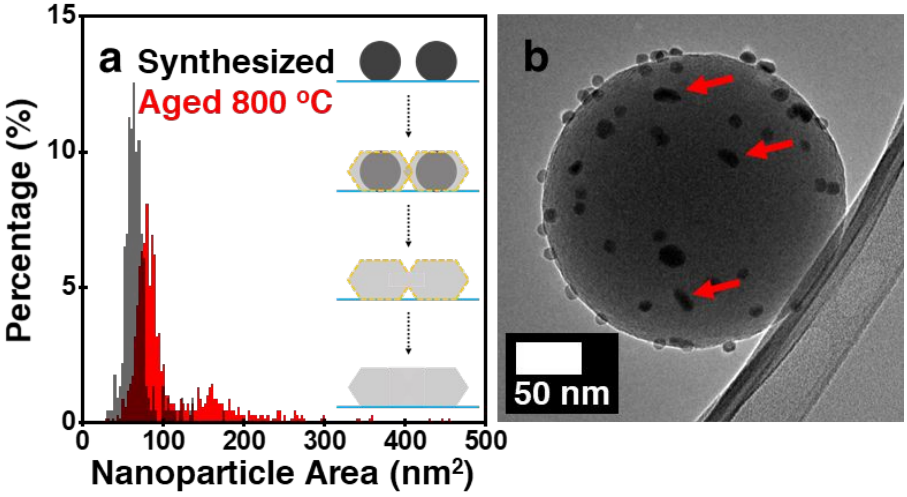

Figure 3. Particle Size Distribution Analysis Reveals Particle Coalescence. (a) Distribution of particle projected areas for 62-Pd/SiO_2 as-synthesized and after aging at 800 ºC for 5 h in static air (N > 200). (b) Representative TEM image of 62-Pd/SiO_2 after aging at 800 ºC for 5 h in static air. Red arrows point to the formation of NC dimers.

Next, bulk characterization techniques were used on the 8.8 nm Pd/SiO_2 sample to understand the rapid sintering onset at 888 °C. Attenuated Total Reflectance Fourier-Transform Infrared Spectroscopy (ATR-FTIR) measurements were performed on the Pd/SiO_2 samples to understand if SiO_2 chemistry governed the stability of the Pd/SiO_2 nanocomposites (**Supporting Figure S8**). However, no obvious changes in surface chemistry of SiO_2 were observed upon reaching 875 °C, suggesting that changes in surface chemistry of the support are not determining the observed stability behavior.

We therefore studied changes in the Pd oxidation state in order to understand its contribution to the observed sintering behavior. According to procedures developed to preserve the oxidation state in Pd materials, the 8.8 nm Pd/SiO_2 was heated to either 875 °C or 900 °C for 5 h in static air, and rapidly cooled down for analysis to freeze the state of the Pd particles.[21] High

resolution TEM (HRTEM) analysis was performed to understand the oxidation state of the material during the sintering process (**Supporting Figure 9**). While at 875 °C we observe mostly PdO, after 900 °C aging we observe the emergence of metallic Pd in sintered aggregates larger than 25 nm in diameter. Additional proof of the relationship between oxidation state and stability was obtained via X-ray diffraction (**Supporting Figure 9**). Like TEM analysis, while we only observe PdO after aging at 875 °C, we find the emergence of metallic Pd after aging at 900 °C. The fact that metallic Pd is observed only when sintering has occurred indicates that metallic Pd is necessary for high-temperature nanocrystal sintering. Further proof is obtained by performing *in-situ* temperature programmed reduction experiments, where particle growth is only observed after PdO is reduced to Pd (**Supporting Figure 10**).

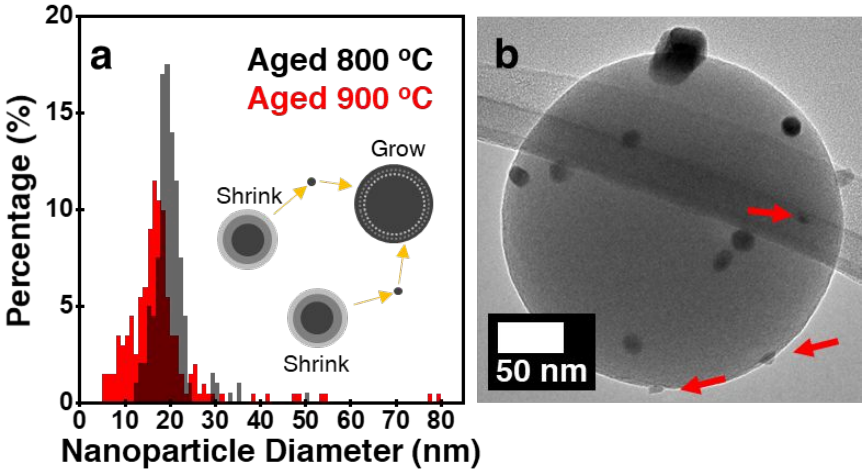

Figure 4. Particle Size Distribution Analysis Reveals Atomic Ripening. Particle size distributions of 14.7 nm Pd/SiO_2 nanocomposite after aging treatments at 800 °C or 900 °C for 5 h in static air (N = 200). (b) Representative TEM image of Pd/SiO_2 after aging at 900 °C for 5 h in static air. Red arrows point to the formation of smaller nanocrystals.

Although we implicate the metallic Pd state in the sintering mechanism above 888 ^{o}C , at this stage it remains unclear whether Ostwald ripening or further particle coalescence leads to this severe nanocrystal sintering. To answer this question, detailed particle size analysis was performed after different aging treatments for the 14.7 nm Pd/SiO_2 sample. After aging at 800 °C or 900 °C for 5 hours in static air, 200 particles were measured along the maximum chord as observed via TEM **(Figure 4, Supporting Figure S11)**, but analysis of projected nanocrystal area yields the same conclusions **(Supporting Figure S12)**. Overall, a shift of the distribution center of mass from ~19 nm to ~16 nm is observed, and a compensatory evolution of much larger 40-80 nm aggregates appear. Most importantly, after aging at 900 °C we observe the emergence of NCs with an average size of less than 10 nm, smaller than the smallest particles present in the 800 °C aged sample, and smaller than the original Pd NCs. The emergence of small NCs is conclusive evidence of Ostwald ripening, where particle size decrease is due to atomic emission and recapture by larger particles, and is uniquely demonstrated by using size-controlled nanocrystal composites. On the other hand, particle coalescence processes could only generate nanocrystals larger than the original nanocrystal building blocks, and would lead to a bimodal size distribution as we saw earlier. However, we cannot exclude that after an initial OR phase, some level of PMC may occur with the formed smaller nanocrystals, while OR continues to proceed. Furthermore, the emergence of smaller nanocrystals, without the entire disappearance of nanocrystals, explains the decrease in NC diameter observed in **Figure 2** for the sample containing large nanocrystals between 800 °C and 900 °C. A schematic inset in **Figure 4a** illustrates how atomic exchange between nanocrystals leads to smaller nanocrystals.

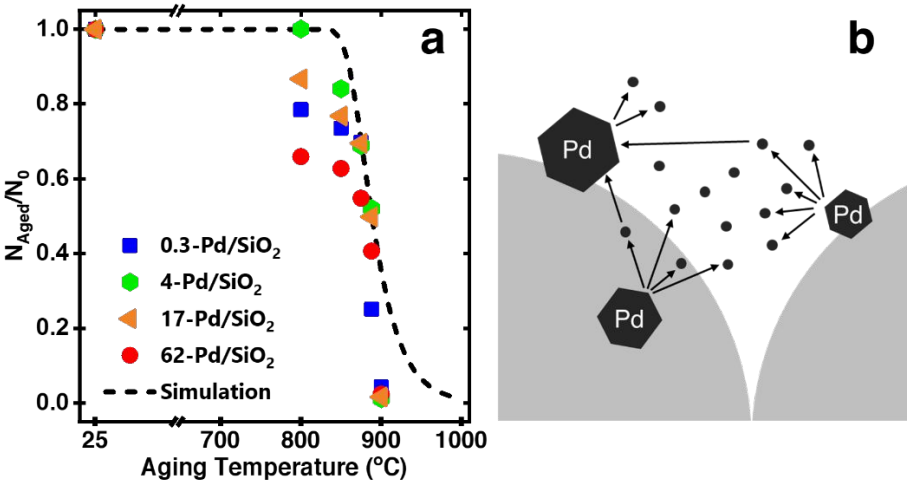

Figure 5. Tracking Nanocrystal Density and the Vapor-Phase Sintering Mechanism. (a) Changes in nanocrystal density for 8.8 nm Pd/SiO_2 nanocomposites as a function of aging temperature. Experimentally measured points are represented with symbols. The vapor phase simulation is represented by the dotted black line, which was performed according to a previously reported protocol.[22] (b) Schematic illustrating vapor-phase atomic exchange between nanocrystals, which shows Pd transfer across SiO_2 spheres.

Additional quantitative particle density analysis was performed for different densities of 8.8 nm Pd/SiO_2 nanocomposites at temperatures up to 900 °C, where change in NC density is represented as the post-treatment nanocrystal density divided by the original nanocrystal density (N_{Aged}/N_0) (Figure 6a). The choice of aging conditions was motivated by the fact that the stability of palladium emissions control catalysts are typically studied under oxidizing conditions at temperatures up to 900 °C.[23] Nanocrystal density decreases slightly between 25 °C and 800 °C due to nanocrystal coalescence (vida supra). Nevertheless, as observed in **Figure 2**, the materials maintain high nanocrystal density until ~875 °C, at which point nanocrystal density rapidly falls.

Similar stability results are identified for Pd/SiO_2 nanocomposites synthesized with commercial Davisil SiO_2, suggesting this remarkable stability is not a unique function of impurities in the SiO_2 prepared with our method, but is instead a more general phenomenon of SiO_2-supported catalysts (**Supporting Figures S13-S14**). Surprisingly, aside from the early oxidative coalescence of nearby crystallites between room temperature and 800 ^oC, there is no obvious trend relating how initial NC density, controllably varied in these four materials, affects aged NC density. Instead the samples follow the same trend independent of initial NC density, and all the nanocomposites fall onto the same curve. Density independence of NC growth means that the distance between NCs is not the most important factor for NC stability, suggesting that atomic diffusion of Pd is rapid and Pd atomic emission is the rate determining step in the Pd sintering process. A similar emission-limited process was recently observed in the case of atomic redispersion for Pd/Al_2O_3 and has been theorized in other works.[6,24] The fact that the 0.3-Pd/SiO_2 sample containing a very low density of particles sinters to such a great extent, leaving behind many empty SiO_2 spheres to form large Pd aggregates, demonstrates the large distances Pd is rapidly traveling (**Supporting Figure S15**). It is extremely challenging to find Pd aggregates in the 0.3-Pd/SiO_2 sample, with an average ratio of 1 Pd aggregate per 300 SiO_2 spheres, suggesting that Pd traverses up to 1 micron within the prolonged sintering process.

Given the remarkable high-temperature stability of the Pd/SiO_2 nanocomposites, and the atomic nature of the sintering process across SiO_2 spheres, a vapor-phase sintering process was hypothesized. Although little quantitative analysis of vapor-phase sintering exists in the experimental literature, significant efforts in analyzing these processes have been pursued via simulations and modeling.[25] By implementing recently developed simulations for vapor-phase sintering processes, we modeled changes in nanocrystal density due to a vapor-phase sintering

process of metallic Pd as a function of temperature, in the absence of any contributions from surface atomic processes or particle migration and coalescence processes. Vapor-phase ripening simulations were performed using a mean-field model for Ostwald ripening, which assumes a constant background pressure of the migrating species.[22] These vapor-phase simulations are represented as a dashed line in **Figure 5**. It is important to note that the developed vapor-phase simulation is independent of nanocrystal spatial distribution due to the assumption that Pd diffusion in the gas phase is more rapid than emission into the gas phase; this assumption is consistent with our experimental observations showing that change in nanocrystal density is independent of the initial state. Theoretical works often study atomic processes in a similar emission-limited regime, even for *surface* OR process.[8,26] Furthermore, we assume that there are no strong adsorbates on the metallic Pd atoms for this analysis, as stable PdO_x moieties have not been posited and experimentally verified.[27]

Sensitivity of this vapor-phase simulation to slight variations in nanocrystal surface energy are plotted in **Supporting Figure S16**. In these simulations, the Gibbs-Thompson equation is used to model the size-dependent nanocrystal energies, and adhesion energies, while important in general, are neglected due to the known weak interactions of SiO_2 supports.[28,29] Overall, experimentally measured changes in nanocrystal density match well with its loss simulated via a vapor-phase sintering mechanism. Vapor pressure calculations of metallic Pd at 900 °C reveal that each NC emits 4 times its total volume of atoms within a 5 hour aging experiment, each NC emitting 5 atoms each second (**Supporting Figure S17**). Emitted gas-phase Pd atoms would have a root mean square velocity of 524 m s^{-1} at 900 °C, suggesting that it would take a Pd atom 442 picoseconds (ps) to travel 232 nm between SiO_2 spheres. Compared to an atomic emission rate of 5 atoms s^{-1}, it is clear that atomic emission, rather than vapor-phase or surface diffusion, is the

rate-determining sintering step. However, as we did not experimentally measure gaseous Pd atoms, we therefore cannot confirm that the process is purely vapor-phase, or without some contribution from the surface process. However, this analysis shows that any surface atomic processes occurring are either (1) occurring at low rates, or (2) governed by emission kinetics very similar to that of emitting a Pd atom directly into the gas phase. Either way, the results demonstrate a sintering process governed at high temperatures by emission-limited atomic ripening processes.

Surprisingly, the vapor-phase sintering model predicts nanocrystal growth at 700-800 °C for 3.0 nm Pd **(Supporting Figure S16)**, yet experimentally we observe stability until 875 °C **(Figure 2)**. Although these smallest nanocrystals seem to achieve stability past the vapor-phase limit, this unexpected result can be explained by understanding the role of oxidation state in the sintering process. At temperatures between 700 °C and 875 °C, particles are still oxidized as PdO, and therefore do not have sintering behavior governed by vapor phase processes of metallic Pd.[30] However, when these particles reduce to metallic Pd at 888 °C, we observe rapid loss of almost all particle density, at which point the sintering is dominated by atomic processes. At this point, it becomes extremely challenging to observe Pd aggregates, and only 1-3 Pd aggregates were found after aging at 900 °C, although the aggregates were at least 20 nm in size. Given the satisfactory match between experiments and simulations, the data suggests that atomic surface processes are likely not occurring to an extent as to dominate the nanocrystal growth process.

Au/SiO_2 Nanocomposites. To probe the generality of the vapor-phase sintering mechanism, we also studied particle growth in Au/SiO_2 materials. Au catalysts are heavily investigated for several applications, although material stability is a well-established issue.[3] Previous works, despite identifying the higher stability of Au/SiO_2 catalysts compared to other

supports, did report a noticeable growth of 2.5 nm Au particles to 6.5 nm when treated in air at 700 °C.[31] Numerous nanostructured support motifs have been developed to increase the stability of Au catalysts.[14,32–37] Here, similar temperature-dependent stability studies were performed on colloidally-synthesized Au/SiO_2 nanostructures, where nanocrystal density was tracked against aging temperature. The average number of Au NCs per SiO_2 sphere was 2.2 in the as-synthesized material. Surprisingly, Au NC density remains constant up to 800 °C, at which point nanocrystal density dropped by a factor of five as temperature approached 900 °C. This data indicates that Au/SiO_2 materials are stable until at least 800 °C, and then they begin to undergo processes of particle growth similar to what was described for Pd. Note that we at low temperatures we observe no loss of density, as no particle coalescence would occur at these low NP densities. Representative TEM images of the Au/SiO_2 as-synthesized (**Figure 6a**) and aged at 800 °C (**Figure 6b**) demonstrate that the small size of the Au NCs was maintained even when multiple NCs coexist on the same SiO_2 sphere. Quantitatively, average size changes minimally, from the 7.8 nm Au starting material to 7.5 nm Au after aging (**Supporting Figure S18**). The stability is quantitatively predicted via simulation of the vapor-phase sintering mechanism, which is also plotted in **Figure 6c**. Au does not form a stable oxide but remains metallic up to high temperatures, which is why the vapor-phase mechanism in this case very well explains the behavior.

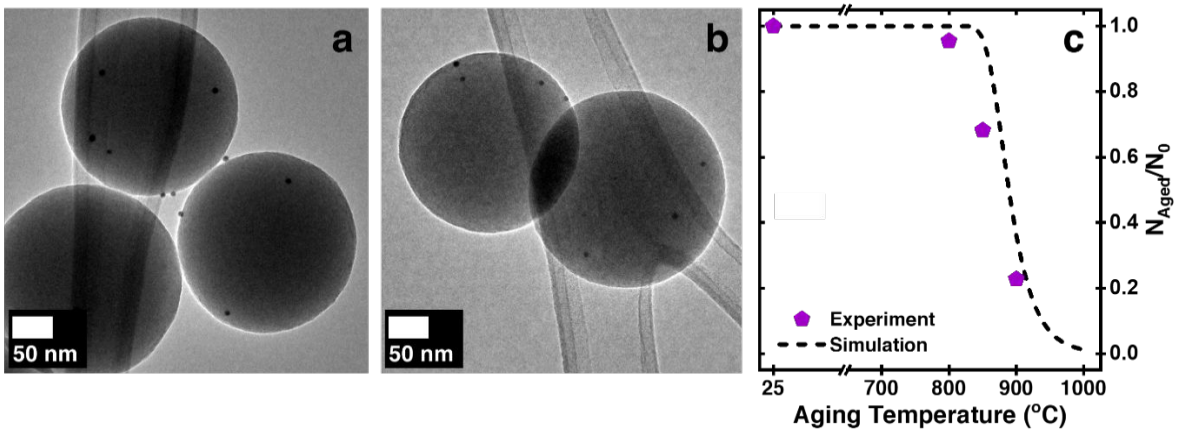

Figure 6. **Vapor-Phase Sintering of Au/SiO_2.** (a) Representative TEM images of Au/SiO_2 (a) as-synthesized and (b) after aging treatment at 800 °C for 5 h in static air. (c) Experimental and simulated NC density versus aging temperature for the Au/SiO_2 nanocomposites.

The high-temperature stability of the Au nanocomposite, which can be explained by vapor-phase sintering processes, is surprising given that the vast efforts put forth to design nanostructured Au catalysts, which would produce barriers to surface processes, but not necessarily vapor processes. We attribute previous works showing drastic sintering of Au-based catalysts to different supports or the presence of byproducts from the synthesis that could undermine Au stability with temperature. Furthermore, in many studies showing Au sintering at lower temperatures, Au NCs may be separated by trivially small distances of ~1-2 nm where processes such as directed migration of adjacent particles within such small proximities may occur.[37,38] In literature examples where control catalysts are compared to encapsulated materials, it is likely that the control material does not contain the exact same nanocrystal size distribution as the encapsulated sample, which may lead to confounding effects in understanding catalyst stability. Nevertheless, there still exist many studies toting the encapsulation of Au for enhanced stability under static calcination conditions.[14,39–41] Here we demonstrate that 'unencapsulated' Au NCs on SiO_2

maintain their stability up to 800 °C in static furnace calcination, at which point they sinter in a process quantitatively consistent with a vapor-phase atomic mechanism. This method can therefore be generalized and extended to several other systems to understand their deactivation behavior.

Conclusions. In this work, we demonstrate how to synthesize powder nanocomposites with precise and independent control of nanocrystal size and nanocrystal spatial distribution. These materials are not only highly stable, but represent important tools in providing fundamental understanding and atomistic insight into nanocrystal sintering mechanisms. By using size-controlled nanocrystal materials, we can deconvolute the spatial extents and severity of entire nanocrystal coalescence from atomic Ostwald ripening processes. These processes are uniquely observed in size-control NC composites through changing particle size distributions. Particle coalescence is demonstrated through the formation of a bimodal particle size distribution, while Ostwald ripening is demonstrated via the emergence of small nanocrystals. Nanocrystal densities are controlled and tracked throughout the aging process, and experimentally measured nanoparticle densities are in quantitative agreement with simulations based on the vapor pressure of Pd and Au metals. The work also demonstrates that appropriate conditions can stabilize metals well beyond what is reported in the literature.

Materials and Methods

Material Synthesis. Pd NCs were synthesized according to prior work.[24] ~18g of SiO_2 spheres were synthesized in a scaled up batch synthesis, according to the following procedure: 72 mL MilliQ H_2O was mixed with 400 mL EtOH (Gold Shield), which was heated to 75 °C and maintained at that temperature for 15 min. Next, 67 mL of NH_4OH (28 – 30%) was added,

temperature quickly fell to 65 ^{o}C, at which point 60 mL tetraethyl orthosilicate (TEOS, 98% Aldrich) was quickly added under vigorous stirring. The solution immediately turned pearly white, and the reaction was completed after 10 minutes. SiO_2 spheres were stored in solution and only isolated as a solid directly prior to use.

Extensive effort was taken to synthesize composite materials with controlled NC size and spatial distribution. In short, 1.52 mL (50 mg) of colloidal SiO_2 from the mother solution (H_2O/EtOH/NH_3) was isolated by centrifugation at 8000 rpm for 10 min. The recovered powder was dried in a centrifuge vial upside down for 10 min, and then redispersed in 15 mL toluene via sonication and vortexing. At this point, the SiO_2 spheres disperse poorly in toluene, and quickly precipitated. The powder was isolated again at 8000 rpm for 3 min, and redispersed in 35 mL of a 15 vol. % EtOH/toluene solution, which dispersed the SiO_2 well. The desired amount of Pd NPs, precipitated once with EtOH and isopropanol (IPA), was redispersed in 5 mL of toluene, and added dropwise to the stirring SiO_2 solution over a period of 5 minutes. This dark mixture was allowed to stir for 30 min, at which point the composite materials were isolated by centrifugation at 8000 rpm for 3 min, and dried overnight at 80 ^{o}C. These materials were sieved through an 80 μm mesh prior to thermal stability testing.

Thermal Aging Experiments and Statistics. Typically, four small ceramic crucibles (each with ~5 mg of catalyst) were placed near the center of a box furnace, and all were heated simultaneously. The samples were subjected to a 3 ^{o}C min^{-1} ramp rate up to the calcination temperature, followed by a five hours isothermal treatment, and finally ramped back down at 3 ^{o}C min^{-1} to room temperature. Without further treatment, the samples were dry-loaded onto a C/Cu TEM grid for analysis. In cases where rapid cool-down was used, (i.e. Figure 3), the furnace was carefully

opened, and the crucible was extracted directly with large tongs and cooled by sitting in ambient air. Control experiments demonstrated that this rapid isolation was crucial, as slow cooldown at 3 $^{o}C\ min^{-1}$ would lead to a sample that was completely oxidized. Cooling rates only effected the nanocrystal oxidation states, and similar sintered particle sizes were observed with either the fast or slow cooling rates. Unless noted, at least 100 SiO_2 spheres were analyzed to get density statistics, and at least 100 NCs were measured to obtain NC size statistics. For area statistics, the ImageJ outline function was used which calculates enclosed areas in designated polygons. 100 NCs were not able to be counted for the 3.3 nm Pd/SiO_2 sample aged at 900 ^{o}C due to the small density of NCs on the surface after sintering.

Monte Carlo Simulations of Nearest Neighbor Nanoparticle Distances (Supporting Figure S8) and Particle per Bead Distributions (Supporting Figure S13). Monte Carlo simulations were performed using standard MATLAB functions. To calculate nearest neighbor distances, an ensemble of at least one thousand SiO_2 was populated with randomly distributed nanoparticles (i.e. 4, 17, or 62 per bead), according to a known algorithm (http://mathworld.wolfram.com/SpherePointPicking.html). Next, a two-dimensional matrix of all interparticle distances (greater circle distances) across the spherical surface was calculated. For each nanoparticle, the smallest nearest neighbor distance was selected. By collecting these nearest neighbor distances for thousands of nanoparticles on thousands of spheres, a histogram of nearest neighbor distances was compiled.

Vapor-Phase Simulations

Vapor-phase ripening simulations were performed using a mean-field model for Ostwald ripening, which assumes a constant background pressure of the migrating species.[22,42] Particle-size dependent vapor pressures were calculated using the Gibbs-Thomson equation with experimental values for both the surface free energies of Pd and Au and their temperature dependent bulk vapor pressures (see Table S3 in the supporting information). The sticking coefficient of the atoms on the metallic surfaces is assumed to be 1. The simulations were initialized with a discretized particle distribution according to a normal distribution, which is centered at the mean diameter and is cut off at values larger than 3 times the standard deviation. Experimental mean diameters and standard deviations of the SiO_2-supported nanocrystals, as indicated in Fig. 1, were used. The discretization is based on 1000 bins to ensure a smooth particle size distribution. The simulated time is 5 h with a time step that is restricted to be below 0.027 s.

ACKNOWLEDGEMENTS. We gratefully acknowledge support from the US Department of Energy, Chemical Sciences, Geosciences and Biosciences Division of the Office of Basic Energy Sciences, via grant no. DE-AC02-76SF00515 to the SUNCAT Center for Interface Science and Catalysis. E.D.G. acknowledges support from the National Science Foundation Graduate Research Fellowship under Grant DGE-1656518. M.C. acknowledges support from the School of Engineering at Stanford University and from a Terman Faculty Fellowship. Part of this work was performed at the Stanford Nano Shared Facilities (SNSF), supported by the National Science Foundation under award ECCS-1542152. E.M.D. and P.N.P. acknowledge support from the state of Baden-Württemberg, Germany through bwHPC (bwunicluster and JUSTUS, RV bw16G001 and bw17D011) and financial support from the Helmholtz Association.

Author contributions. E.G. and M.C. conceived the idea for the study. E.G. prepared the samples with contribution from E.Z.C., N.T., A.J. and T. T. E.G. and A.A. performed the XPS and TEM characterization. E.M.D. performed vapor-phase simulation with supervision from P.N.P. M.C. supervised the entire project. E.G. wrote the manuscript with contribution from all authors.

Competing financial interests. The authors declare no competing financial interests or conflicts of interest.

References.

[1] S. L. Scott, *ACS Catal.* **2018**, *8*, 8597.

[2] M. D. Argyle, C. H. Bartholomew, *Catalysts* **2015**, *5*, 145.

[3] E. D. Goodman, J. A. Schwalbe, M. Cargnello, *ACS Catal.* **2017**, *7*, 7156.

[4] Robert J. Farrauto, *Science* **2012**, *337*, 659.

[5] T. W. Hansen, A. T. Delariva, S. R. Challa, A. K. Datye, *Acc. Chem. Res.* **2013**, *46*, 1720.

[6] S. R. Challa, A. T. Delariva, T. W. Hansen, S. Helveg, J. Sehested, P. L. Hansen, F. Garzon, A. K. Datye, *J. Am. Chem. Soc.* **2011**, *133*, 20672.

[7] A. K. Datye, Q. Xu, K. C. Kharas, J. M. Mccarty, *Catal. Today* **2006**, *111*, 59.

[8] S. C. Parker, C. T. Campbell, *Phys. Rev. B* **2007**, *75*, 035430.

[9] J. Liu, Q. Ji, T. Imai, K. Ariga, H. Abe, *Nat. Sci. Reports* **2017**, 1.

[10] X. Yang, Q. Li, E. Lu, Z. Wang, X. Gong, Z. Yu, Y. Guo, L. Wang, Y. Guo, W. Zhan, J. Zhang, S. Dai, *Nat. Commun.* **2019**, *10*, 1.

[11] L. De Rogatis, M. Cargnello, V. Gombac, B. Lorenzut, T. Montini, P. Fornasiero, *ChemSusChem* **2010**, *3*, 24.

[12] Y. Xu, J. Ma, Y. Xu, L. Xu, L. Xu, H. Li, H. Li, *RSC Adv.* **2013**, *3*, 851.

[13] A. J. Forman, J. Park, W. Tang, Y. Hu, G. D. Stucky, E. W. McFarland, *ChemCatChem* **2010**, *2*, 1318.

[14] P. M. Arnal, M. Comotti, F. Schuth, *Angew. Chemie - Int. Ed.* **2006**, *45*, 8224.

[15] S. H. Joo, J. Y. Park, C. Tsung, Y. Yamada, P. Yang, G. A. Somorjai, *Nat. Mater.* **2009**, *8*, 126.

[16] G. Prieto, J. Zecevic, H. Friedrich, K. Jong, P. Jongh, *Nat. Mater.* **2013**, *12*, 34.

[17] X. Yan, X. Wang, Y. Tang, S. Zou, R. Li, X. Peng, S. Dai, J. Fan, *Chem. Mater.* **2013**, *25*, 1556.

[18] M. T. Bore, H. N. Pham, E. E. Switzer, T. L. Ward, A. Fukuoka, A. K. Datye, **2005**, 2873.

[19] L. DeRita, J. Resasco, S. Dai, A. Boubnov, H. V. Thang, A. S. Hoffman, I. Ro, G. W. Graham, S. R. Bare, G. Pacchioni, X. Pan, P. Christopher, *Nat. Mater.* **2019**, *18*, 746.

[20] C. T. Campbell, S. C. Parker, D. E. Starr, *Science* **2002**, *298*, 811.

[21] H. Xiong, K. Lester, T. Ressler, R. Schlögl, L. F. Allard, A. K. Datye, *Catal. Letters* **2017**, *147*, 1095.

[22] P. N. Plessow, F. Abild-Pedersen, *ACS Catal.* **2016**, *6*, 7098.

[23] J. G. McCarty, G. Malukhin, D. M. Poojary, A. K. Datye, Q. Xu, *J. Phys. Chem. B* **2005**, *109*, 2387.

[24] E. D. Goodman, A. C. Johnston-peck, E. M. Dietze, C. J. Wrasman, A. S. Hoffman, F. Abild-pedersen, S. R. Bare, P. N. Plessow, M. Cargnello, *Nat. Catal.* **2019**.

[25] E. M. Dietze, P. N. Plessow, *J. Phys. Chem. C* **2018**, *122*, 11524.

[26] Y. G. Beien Zhu, Rui Qi, Lina Yuan, *Nanoscale* **2020**, *12*, 19142.

[27] R. Ouyang, J. Liu, W. Li, *J. Am. Chem. Soc.* **2013**, *135*, 1760.

[28] C. T. Campbell, Z. Mao, *ACS Catal.* **2017**, *7*, 8460.

[29] S. Soled, *Science (80-.).* **2015**, *350*, 1171.

[30] Y. H. Chin, E. Iglesia, *J. Phys. Chem. C* **2011**, *115*, 17845.

[31] N. Masoud, T. Partsch, K. P. De Jong, P. E. De Jongh, *Gold Bull.* **2019**, *52*, 105.

[32] B. K. Min, W. T. Wallace, D. W. Goodman, *J. Phys. Chem. B* **2004**, 14609.

[33] A. Beck, A. Yang, A. R. Leland, A. R. Riscoe, F. A. Lopez, E. D. Goodman, M. Cargnello, *AIChE J.* **2018**, *64*, 3159.

[34] M. T. Bore, H. N. Pham, T. L. Ward, A. K. Datye, *Chem. Commun.* **2004**, 2620.

[35] Y. Chi, H. Lin, C. Mou, *Appl. Catal. A Gen.* **2005**, *284*, 199.

[36] X. Cao, J. Zhou, H. Wang, S. Li, W. Wang, G. Qin, *J. Mater. Chem. A* **2019**, *7*, 10980.

[37] W. Yuan, D. Zhang, Y. Ou, K. Fang, B. Zhu, H. Yang, T. W. Hansen, J. B. Wagner, Z. Zhang, Y. Gao, Y. Wang, *Angew. Chemie - Int. Ed.* **2018**, *57*, 16827.

[38] A. D. Benavidez, L. Kovarik, A. Genc, N. Agrawal, E. M. Larsson, T. W. Hansen, A. M. Karim, A. K. Datye, *ACS Catal.* **2012**, *2*, 2349.

[39] C. Radloff, N. J. Halas, *Appl. Phys. Lett.* **2001**, *79*, 674.

[40] C. Lin, X. Liu, S. Wu, K. Liu, C. Mou, *J. Phys. Chem. Lett.* **2011**, *2*, 2984.

[41] J. Chen, R. Zhang, L. Han, B. Tu, D. Zhao, *Nano Res.* **2013**, *6*, 871.

[42] P. Wynblatt, N. A. Gjostein, *Acta Metall.* **1976**, *24*, 1165.

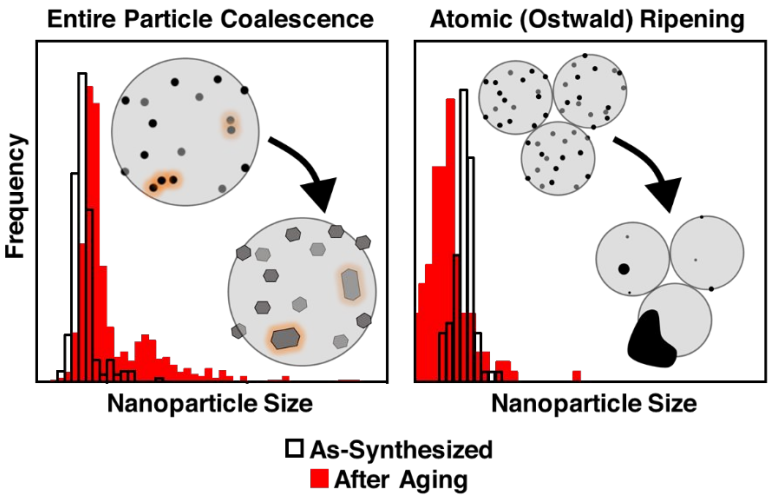
Entire Particle Coalescence
Atomic (Ostwald) Ripening
Frequency
Nanoparticle Size
Nanoparticle Size
As-Synthesized
After Aging